Seismic anisotropy across the Kunlun fault and their implications for northward transforming lithospheric deformation in northeastern Tibet

Chenglong Wu [a,b], Tao Xu [a,c,*], José Badal [d], Zhenbo Wu [a,b], Jiwen Teng [a]

[a] State Key Laboratory of Lithosphere Evolution, Institute of Geology and Geophysics, Chinese Academy of Sciences, Beijing, 100029, China
[b] University of Chinese Academy of Sciences, Beijing, 100049, China
[c] CAS Center for Excellence in Tibetan Plateau Earth Sciences, Beijing, 100101, China
[d] Physics of the Earth, Sciences B, University of Zaragoza, Pedro Cerbuna 12, 50009 Zaragoza, Spain

ARTICLE INFO

ABSTRACT

The northeastern Tibet is produced by the far field effects of the India–Eurasia collision in Late Cenozoic. As the southern boundary of the northeastern Tibet the Kunlun fault is a key to understand how the Tibetan Plateau transforms lithospheric deformation outward. Using a northeast–southwest trending seismic array deployed in Songpan–Ganzi, Qaidam–Kunlun, and Qilian blocks, we measured SKS/SKKS wave splitting parameters at 15 broadband seismic stations to study the variation in anisotropy across the Kunlun fault and among these blocks. The average splitting parameters of the southern segment in Songpan–Ganzi block are N132.3°E and 1.1 s respectively, and those of the northern segment in Qilian block are N103.8°E and 0.98 s, interfered with the middle segment in Qaidam–Kunlun block with a smaller average delay time 0.63 s. A schematic geodynamic model is used to explain the distinct features among these blocks. Weak anisotropy suggests the strong lithosphere of Qaidam–Kunlun block with negligible deformation. A counterclockwise rotation of the fast polarization direction of about 30° from Songpan–Ganzi block to Qilian block is produced by a ladder-shaped strong Qaidam–Kunlun block.

© 2015 Elsevier B.V. All rights reserved.

1. Introduction

The Tibetan Plateau is a privileged place for understanding the continental collision and mountain building processes. A series of geodynamic models have been proposed to explain how the topography of the Tibetan highlands is formed and maintained. Summarizing, they can be classified into: 1) the rigid block model, in which discrete tectonic blocks, with little internal deformation, are being extruded eastward between large lithospheric-scale strike-slip faults (Tapponnier et al., 1982, 2001); 2) the thin viscous sheet model for continental deformation, according which the entire Tibetan lithosphere uniformly shortens and thickens as a thin viscous sheet in response to the India–Eurasia collision (England and McKenzie, 1982); 3) the model of ductile flow of the middle-to-lower crust, which segregates deformation between the upper crust and the mantle lithosphere (Clark and Royden, 2000; Royden, 1996).

As the northern terminus of contiguous deformation, the NE Tibetan Plateau is an important area for investigating the far field effects of the India–Eurasia collision (Dayem et al., 2009; Tian and Zhang, 2013; Yin et al., 2007, 2008a, 2008b). Active overthrusting spreads widely over a large area ~500,000 km² in the NE corner of Tibet (Tapponnier et al., 2001). Bounded by active thrusts, large scale mountain ranges with hundreds of kilometers long and tens of kilometers wide are deformed as NW-trending ramp anticlines (Tapponnier et al., 1990). The accumulated regional shortening occurs at a rate of 1.5 cm/year in direction N30°E from the Late Neogene (Meyer et al., 1998); it is only slightly less than the shortening across the Himalaya about 2 cm/year (Tapponnier et al., 2001). The presence of abundant strike–slip faults including the Kunlun fault indicates the NE Tibet represents a key area of geodynamic interest for the India–Eurasia collision (Meyer et al., 1998).

Measurements of seismic anisotropy can provide insight into the nature of the finite strain field in the lithosphere and uppermost mantle defined by the fast polarization direction and delay time because the anisotropy appears to result from the strain-induced lattice preferred orientation of anisotropic minerals, such as olivine and orthopyroxene (Silver and Chan, 1991). Previous studies have used shear-wave splitting analysis to investigate upper-mantle anisotropy beneath NE Tibet and adjacent areas (Chang et al., 2008; Eken et al., 2013; Leon Soto et al., 2012; Li et al., 2011a, 2011b; Wang et al., 2008; Zhang et al., 2012; Zhao et al., 2011). Wang et al. (2008) concluded that the surface and mantle deform coherently, arguing for strong crust-mantle coupling (including NE Tibet). A SKS splitting survey line covering a broad
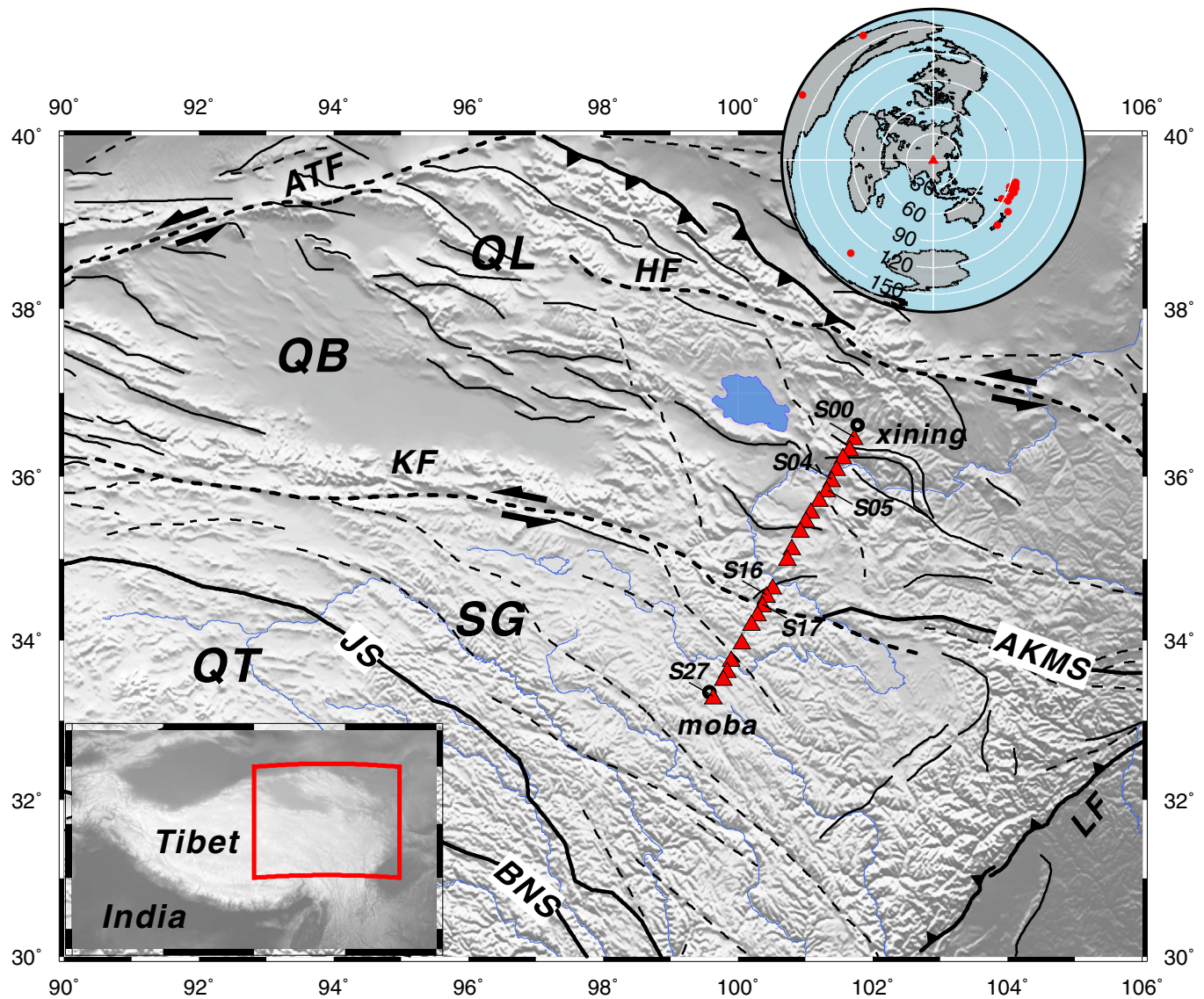
Fig 1. Tectonic map of northeastern Tibet showing the main geological features in the region. The study area appears enclosed within a small rectangle in the bottom left inset. In this study we used the northeast–southwest trending seismic array deployed between the cities of Xining (to north) and Moba (to south) that crosses the Kunlun fault. The locations of the broadband seismic stations belonging to the array are indicated by red triangles across the eastern Kunlun Mountains. Key to symbols: BNS, Bangong–Nujiang Suture; JS, Jinsha Suture; AKMS, Animaqing–Kunlun–Muztagh Suture; QT, Qiangtang Block; SG, Songpan–Ganzi Block; QB, Qaidam–Kunlun Block; QL, Qilian Block; LF, Longmenshan Fault; KF, Kunlun Fault; HF, Haiyuan Fault; ATF, Altyn Tagh Fault. The top right inset shows the location of the teleseismic events selected for this study.

Table 1
Seismic events used in this study.

Event ID	Date	Time	λ_E (°)	φ_N (°)	H (km)	M_w	No. of observations
20103620834	2010/12/28	08:34:17.55	−179.8020	−23.4070	551.00	6.30	6
20110010956	2011/01/01	09:56:58.12	−63.1360	−26.8030	576.80	7.00	1
20110050646	2011/01/05	06:46:14.63	171.6310	−22.2600	112.20	6.10	2
20110231915	2011/01/23	19:15:42.67	−176.2920	−20.3350	236.10	5.90	6
20110240102	2011/01/24	01:02:02.03	−173.5100	−19.2040	16.20	5.70	2
20110310603	2011/01/31	06:03:27.30	−175.6220	−22.0090	76.00	6.00	7
20110342025	2011/02/03	20:25:15.89	−173.0680	−15.5110	10.00	6.00	1
20110521057	2011/02/21	10:57:52.41	178.3940	−26.1420	558.10	6.60	6
20110522351	2011/02/21	23:51:42.35	172.6800	−43.5830	5.90	6.10	5
20110651231	2011/03/06	12:31:59.78	−69.3620	−18.0210	118.00	6.30	2
20110651432	2011/03/06	14:32:36.08	−27.0630	−56.4220	87.70	6.50	2
20110710119	2011/03/12	01:19:07.20	−173.2050	−16.7240	14.00	5.80	2
20110852249	2011/03/26	22:49:41.47	−179.4060	−15.8510	10.00	6.10	1
20110900011	2011/03/31	00:11:58.30	−177.5170	−16.5410	15.50	6.40	3
20110931407	2011/04/03	14:07:09.33	−178.5850	−17.6420	551.70	6.40	8
20110950410	2011/04/05	04:10:07.19	−178.5950	−17.6620	552.40	5.80	2
20111050206	2011/04/15	02:06:26.80	−173.2320	−15.2770	7.00	5.80	6
20111052146	2011/04/15	21:46:22.70	−175.3630	−18.6910	216.30	5.70	5
20111081303	2011/04/18	13:03:02.73	179.8740	−34.3360	86.00	6.60	12

Nomenclature: λ_E, latitude; φ_N, longitude; H, focal depth; M_w, moment magnitude.

area in northeastern Tibet (Leon Soto et al., 2012) confirmed this result and demonstrated fast polarization directions subparallel to the left-lateral maximum shear direction in this part of Tibet. Furthermore, Zhang et al. (2012) suggested two different patterns of upper-mantle deformation north and south of the Kunlun fault both on the basis of crust-mantle coupling. Nonetheless, Li et al.

(2011b) explained the anisotropy observations near Xining and surroundings by a model of two anisotropic layers that indicates the decoupling of crust and mantle.

The Kunlun fault marks the northern boundary of the Tibetan Plateau for nearly 1500 km along strike, delineating a transition from a continuous, low-relief, high elevation plateau to the south to a
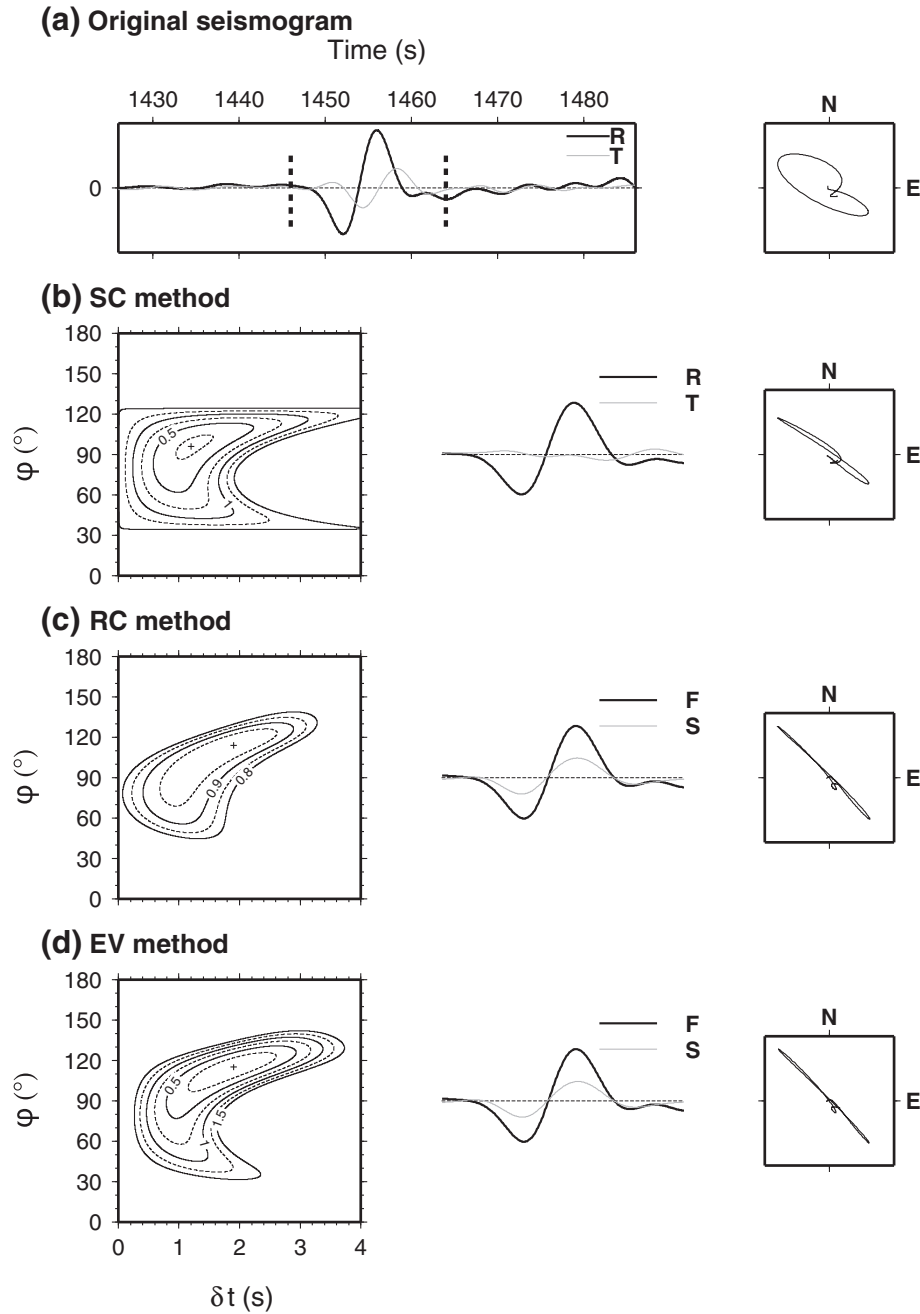

Fig. 2. Example of SKS-wave splitting measurement for the source-station pair integrated by the event 20111081303 occurred on April 18, 2011 (Table 1) and the station S02. (a) Original seismograms (left panel) with the radial (bold line, R) and transverse (gray thin line, T) components of the ground motion, and selected time window (bounded by two vertical dashed lines). The initial particle motion can be seen in the right-hand panel. (b) Splitting parameter measurement using the SC method. The left panel is the contour map of transverse energy; the cross marks the best-fitting splitting parameters that are φ = 96°, δt = 1.2 s. The middle panel shows the corrected radial (bold line, R) and transverse (gray thin line, T) components of the motion. The corrected particle motion is shown in the right-hand panel. (c) Splitting parameters calculated by the RC method. The best-fitting splitting parameters are φ = 114°, δt = 1.9 s (marked by the cross in the contour map drawn in the left panel). The middle panel shows the corrected (rotated and time-shifted) fast and slow components of the motion (F and S, respectively), while the particle motion is plotted in the right-hand panel. (d) Splitting parameters calculated by the EV method. The best-fitting splitting parameters are φ = 115° and δt = 1.9 s (cross in the contour map drawn in the left panel). The fast (F) and slow (S) components of the motion are plotted in the middle panel, and the particle motion in the right-hand panel.

northern domain characterized by active high mountain ranges and intramontane basins (Kirby et al., 2007). The East Kunlun fault system only became active as a strike–slip system during the last 7 Ma, with a total slip of 75 km (Fu and Awata, 2007) and a Late Quaternary slip rate of >10 mm/year in the west to <2 mm/year at the tip in the east (Kirby et al., 2007; van der Woerd et al., 2000, 2002). The fault, which follows the trace of the AKMS, represents one of the key structural elements in the active deformation field of Eurasia (Avouac and Tapponnier, 1993). This study is aimed to characterize shear-wave splitting pattern across the Kunlun fault (~100°E) in order to better understand the upper mantle deformation in NE Tibet. Some work utilizing the active and passive source data respectively in this survey line has been done (Deng et al., in press; Wu et al., in press; Xu et al., 2014; Zhang et al., 2011). The explored area contains highly deformed orogenic belts, such as the Songpan–Ganzi Block (SG) and the Qilian Orogen (Fig. 1). The results obtained through shear-wave splitting analysis based on new data extracted from a passive-source seismic experiment, may be key to get a more detailed picture of the seismic anisotropy in the upper mantle in NE Tibet and shed new light on the geodynamic process governing this region.

2. Data and method

The northeast–southwest trending broadband seismic array was deployed between the cities of Xining (to north) and Moba (to south) between November 2010 and June 2011 including 22 seismograph stations composed of Reftek-72A data loggers and Guralp CMG-3ESP sensors (Fig. 1). The array extended about 400 km with a station space of 10–15 km. Five stations (S00–S04) were installed in the Qilian Block, nine stations (S05–S16) in the Qaidam–Kunlun Block, and eight stations (S17–S27) in the Songpan–Ganzi block.

Clear records of teleseismic SKS and SKKS phases were selected from earthquakes with Mw magnitude equal to or greater than 5.5 and epicentral distance ranging from 85° to 170°. Most of the events lie in Tonga and adjacent regions (see top right inset in Fig. 1). Only phases with high signal-to-noise ratio on the original trace were considered for analysis, especially SKS phases by its steeper incidence at the receiver. Other phases were rejected to ensure high lateral resolution (including PKS waves that gave unsatisfactory results). A total of 19 seismic events (listed in Table 1) provided high-quality data for shear-wave splitting measurements.

The shear wave splitting analysis method estimates the fast polarization direction (φ) and the delay time between the fast and slow waves (δt). These two parameters indicate the preferred mineral orientation and the extent of anisotropy (Silver and Chan, 1991; Silver and Savage, 1994). Core–mantle refracted phases, such as SKS and SKKS, are used to infer the preferred lattice orientation of minerals (mostly olivine) in the anisotropic upper mantle (Savage, 1999; Silver, 1996). To estimate splitting parameters we adopted the method proposed by Tian et al. (2011), which is called 'global minimum transverse energy' (hereafter GM). Unlike the traditional procedure, this method applies a sensor misorientation correction and follows the steps: (1) correction (rotation) of the motion components (hereafter RC; e.g. Bowman and Ando, 1987); (2) minimization of the energy of the reconstructed transverse component (hereafter SC; e.g. Silver and Chan, 1991); and (3) minimization of the eigenvalues of the covariance matrix for the two orthogonal components (hereafter EV; e.g. Silver and Chan, 1991). To mitigate noise effects and enhance the signal-to-noise ratio on splitting measurements, all the adopted bandpass filters had a fixed lower corner frequency of 0.03 Hz to suppress long-period noise and higher corner frequencies varying from 0.2 to 0.5 Hz to remove high-frequency scattering induced by small-scale heterogeneities. A recent study has demonstrated that SKS-wave propagation is strongly influenced by the frequency band (Zhao and Xue, 2015), while most measurements in this study are rather consistent using different bandpass

filters. According to the Fresnel zone effects as interpreted by Alsina and Snieder (1995), low-frequency measurements are sensitive to a larger and deeper anisotropic volume than high-frequency measurements (Chevrot et al., 2004; Favier and Chevrot, 2003; Long and van der Hilst, 2006). The main frequency band is 0.03–0.2 Hz. However, in some cases, due to the less delay time, we chose higher frequency bandpass filters for denoising, especially with the seismograms recorded at some stations located in the middle part of the survey line. Detailed information to this respect is listed in Table S1 (auxiliary material).

An example of the outputs provided by splitting measurements by applying the traditional estimation techniques and the GM method mentioned above is shown in Fig. 2. The example makes reference to the source-station pair integrated by the event 20111081303 occurred on April 18, 2011 (Table 1) and the station S02. The SKS splitting parameters were calculated from the signals generated by this event (drawn in Fig. 2a) within a time window of about 18 s. The splitting parameters are those given by the best-fitting solution to the fast polarization direction (φ) and delay time (δt). This procedure is systematically used in any other case. In the present example, the splitting results are φ = 96°, δt = 1.2 s by the SC method (Fig. 2b), φ = 114°, δt = 1.9 s by the RC method (Fig. 2c) and φ = 115°, δt = 1.9 s by the EV method (Fig. 2d). The inconsistency of the results may indicate a misalignment of the horizontal components. Fig. 3 shows the splitting parameters estimated by the GM method, which make clear a misorientation of θ = 12° when the transverse energy reaches a global minimum, and the splitting parameters provided by the SC method are equal to those given by the EV method. After a sensor realignment, i.e. after rotating the horizontal components 12° clockwise, the splitting parameters supplied by the SC, RC and EV methods become the same, φ = 103°, δt = 1.9 s, as is shown in Fig. 4. In this illustration we can see, from left to right and for each case, the best-fitting solution to the fast direction and delay time (marked by a cross in the left panels), the fast and slow components of the motion and the particle motion.

Only the estimations that satisfied the following conditions were considered as accurate splitting parameters: (1) consistent results by SC and EV methods for global minimum transverse energy (MTE in Fig. 3); (2) elliptic particle motion, similar waveforms of the two
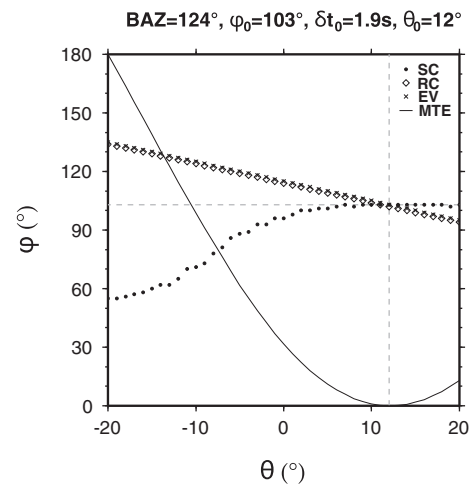

Fig. 3. Variation of the fast polarization direction (φ) depending on the sensor angle (θ) assuming a clockwise rotation of horizontal components. The drawn curves make reference to the same earthquake before mentioned (in Fig. 2) and the methods SC (circles), RC (diamonds) and EV (crosses) with which the splitting parameters (φ and δt) were calculated. The variation of the minimum transverse energy (MTE, thin line) with θ is plotted in the same panel after normalization. When θ = θ₀ = 12°, i.e. with a sensor misorientation of 12° westward, MTE is minimized and the splitting parameters provided by the SC method are equal to those given by the EV method. After a sensor realignment of 12° clockwise, the results from the SC and EV methods become the splitting parameters φ = 103° and δt = 1.9 s.
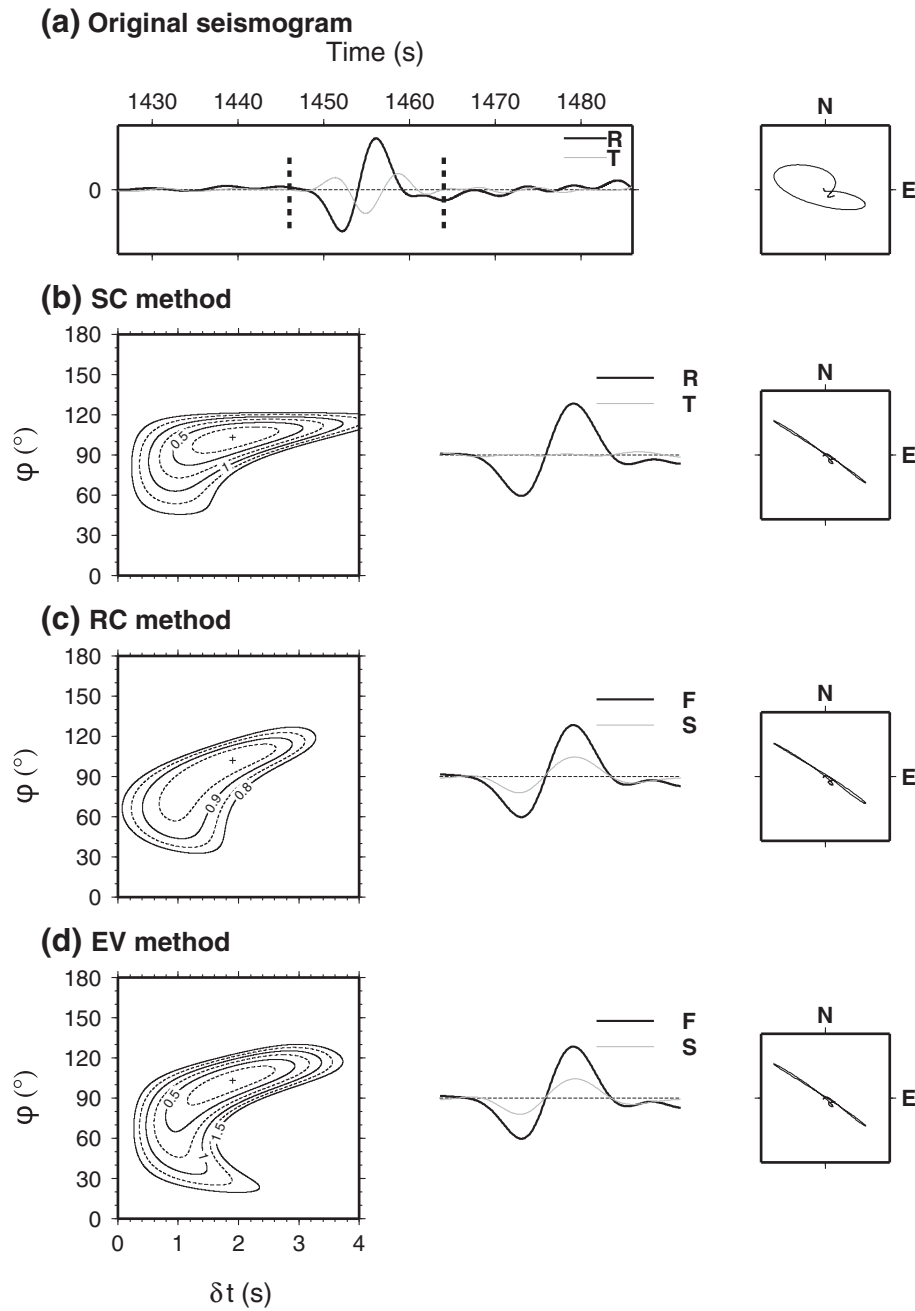
Fig. 4. Same outputs and legends as in Fig. 2, but now with reference to results obtained with a 12° clockwise sensor correction applied to the north and east components of motion before shear-wave splitting measurements. The best-fitting splitting parameters are φ = 103°, δt = 1.9 s using any of the three calculation methods, SC (b), RC (c) and EV (d).

horizontal motion components and clearly linear particle motion after removing the anisotropy effect (Herquel et al., 1999); (3) $\sigma_\varphi <$ 22.5° and $\sigma_{\delta t} < \delta t/2$, where σ_φ and $\sigma_{\delta t}$ are used to describe the 95% confidence interval for φ and δt when applying a method that is affected by the frequency content of the data (Silver and Chan, 1991); (4) |ΔBAZ| ≥ 10°, where |ΔBAZ| denotes the difference in back azimuths of the fast or slow direction and the event (the smaller one). This standard based on the comparison of different signal processing techniques (Long and van der Hilst, 2005; Wüstefeld and Bokelmann, 2007) demonstrates that the methodology of Silver and Chan (1991) is reliable for cases with |ΔBAZ| down to 10°.

We defined the null cases of splitting measurements with the RC and SC methods based on the differences between the results obtained by the two methods (Huang et al., 2011; Wüstefeld and Bokelmann, 2007): the angular difference $\psi = |\varphi_{RC} - \varphi_{SC}|$ for φ

and the ratio $\rho = \delta t_{RC}/\delta t_{SC}$ for δt. The criterion taken is 30° < ψ < 60° and ρ < 0.3.

3. Splitting results

Not all teleseismic events produced useful information and some of them gave null cases of splitting measurements. Despite this drawback we obtained good results at 15 seismograph stations of the array. A total of 54 pairs of splitting parameters including 50 from SKS phases and 4 from SKKS phases were obtained (Table 2). All null cases are listed in Table 3. The individual measurements are shown in Fig. S1 (auxiliary material) with different colors representing SKS and SKKS respectively.

In the north part of the study area, some researchers found a complex anisotropy structure. Li et al. (2011b) reported dependence of

Table 2
SKS and SKKS splitting measurements.

Station	Event ID	BAZ (°)	DIS (°)	φ (°)	σ_φ (°)	δt (s)	$\sigma_{\delta t}$ (s)	Phase
S00	20110521057	119	96	47	5.5	0.70	0.21	SKS
	20110522351	135	103	111	2.5	1.80	0.15	SKS
	20111081303	124	102	94	13.5	1.00	0.31	SKS
S01	20110522351	135	103	115	3.5	1.90	0.31	SKS
	20110710119	106	96	136	13.5	0.80	0.31	SKS
	20111081303	124	101	101	5.0	0.90	0.10	SKS
S02	20110522351	135	103	104	5.5	1.60	0.26	SKS
	20111081303	124	101	103	2.0	1.90	0.10	SKS
S04	20110522351	135	103	118	3.5	1.60	0.31	SKS
	20111081303	124	101	95	6.5	1.20	0.26	SKS
S06	20110521057	118	96	60	9.0	0.40	0.05	SKS
	20111081303	124	101	102	2.0	1.20	0.05	SKS
S07	20110010956	299	164	61	17.5	1.30	0.56	SKKS
	20110521057	118	96	54	10.5	0.70	0.21	SKS
	20111081303	124	101	96	17.5	1.00	0.36	SKS
	20111081303	124	101	77	13.0	1.60	0.46	SKKS
S08	20103620834	115	95	71	20.5	0.40	0.10	SKS
	20110521057	118	96	73	5.5	0.50	0.05	SKS
	20110651231	331	161	91	4.0	1.50	0.15	SKKS
S11	20110521057	118	96	86	8.0	0.50	0.10	SKS
	20111081303	124	101	86	19.0	0.70	0.21	SKS
S12	20110521057	118	96	84	4.5	0.70	0.05	SKS
	20110522351	135	102	102	13.0	0.90	0.26	SKS
S16	20110342025	105	96	156	17.5	1.00	0.31	SKS
	20110852249	108	91	125	5.5	1.40	0.36	SKS
	20110931407	109	93	125	2.5	1.20	0.15	SKS
S17	20110900011	108	93	168	9.5	0.90	0.21	SKS
	20110931407	109	93	124	1.5	1.30	0.10	SKS
	20111050206	105	96	173	4.0	1.10	0.21	SKS
	20111052146	109	96	134	9.5	1.40	0.46	SKS
S19	20110240102	108	98	145	7.0	1.00	0.15	SKS
S21	20103620834	115	95	143	6.0	0.70	0.10	SKS
	20110231915	110	96	147	11.0	0.80	0.10	SKS
	20110310603	111	98	135	1.0	1.30	0.05	SKS
	20110710119	106	97	162	5.5	1.30	0.15	SKS
	20110900011	108	93	157	8.0	1.10	0.15	SKS
	20110931407	109	93	143	6.0	0.90	0.10	SKS
	20110950410	109	93	152	10.0	1.10	0.26	SKS
	20111050206	104	96	144	17.0	1.10	0.36	SKS
	20111052146	108	96	129	4.5	1.50	0.31	SKS
S23	20103620834	115	95	134	8.5	1.00	0.36	SKS
	20110231915	110	96	134	8.5	1.40	0.56	SKS
	20110310603	111	98	129	5.0	1.70	0.41	SKS
	20110900011	108	93	132	4.0	2.00	0.26	SKS
	20110931407	109	93	132	2.0	1.50	0.10	SKS
	20110950410	109	93	138	6.0	1.80	0.36	SKS
	20111050206	104	96	139	5.0	1.40	0.15	SKS
	20111052146	108	96	130	5.0	1.60	0.26	SKS
S27	20103620834	115	95	153	6.0	0.80	0.10	SKS
	20110310603	111	98	152	5.5	0.80	0.10	SKS
	20110651231	324	162	125	3.5	2.00	0.31	SKKS
	20110931407	109	93	128	7.0	1.40	0.46	SKS
	20111050206	104	96	125	1.5	1.80	0.10	SKS
	20111052146	108	96	125	3.5	1.80	0.31	SKS

Nomenclature: BAZ, back-azimuth; DIS, epicentral distance; φ, fast polarization direction; σ_φ, measurement error; δt, delay time; $\sigma_{\delta t}$, measurement error.

Table 3
Summary of null cases.

Station	Event ID	BAZ (°)	DIS (°)	Phase
S00	20111050206	105	95	SKS
S01	20110050646	119	88	SKS
	20110231915	111	96	SKS
	20110310603	112	97	SKS
	20111052146	109	96	SKS
S04	20110240102	108	97	SKS
	20110310603	112	97	SKS
	20110931407	110	93	SKS
S06	20110651432	222	140	SKKS
S07	20110310603	112	98	SKS
	20110931407	110	93	SKS
S08	20110231915	111	96	SKS
	20110931407	110	93	SKS
S11	20103620834	115	95	SKS
	20110231915	111	96	SKS
	20111050206	105	96	SKS
S12	20103620834	115	95	SKS
	20110231915	111	96	SKS
S16	20111081303	124	101	SKS
S17	20110050646	119	88	SKS
	20110310603	111	98	SKS
	20111081303	124	101	SKS
S21	20110651432	221	138	SKKS
	20111081303	124	101	SKS
	20111081303	124	101	SKKS

factors derived from measurement errors. The station average $\bar{x}$ was computed from the N individual measurements weighted by the reciprocal of the variance obtained from the F test, i.e.,

$$\bar{x} = \left(\sum_{i=1}^{N} {}_i x_i \right) \bigg/ \sum_{i=1}^{N} w_i \tag{1}$$

where $w_i = 1/\sigma_i^2$, and x_i is the splitting parameter (φ or δt) for the ith event. We used Eq. (2) as a measure of the degree of consistency among individual measurements from a station, which is defined as (Galassi et al., 2007)

$$\sigma_s = \sqrt{\frac{U_1 U_2}{U_1^2 - U_3}} \tag{2}$$

where, $U_1 = \sum_{i=1}^{N} w_i$, $U_2 = \sum_{i=1}^{N} w_i (x_i - \bar{x})^2$, and $U_3 = \sum_{i=1}^{N} w_i^2$. The averaged SKS splitting measurements for each station are given in Table 4 and plotted in Fig. 5. In this figure we show the shear-wave splitting vectors (fast directions and delay times) obtained in this study together with those extracted from previous research works (Leon Soto et al., 2012; Wang et al., 2008; Zhang et al., 2012).

In order to better understand the anisotropy pattern, we grouped the stations into three groups according to their locations in the different tectonic units (Fig. 6). The stations located in the northern transect of the array, south of the Qilian Block and its vicinity (S00, S01, S02, S04, S06), form the first group (group 1). The stations located in the middle part of the array (S07, S08, S11, S12), in the Qaidam–Kunlun Block, just north of the Kunlun fault, form the second group (group 2). The third group (group 3) of stations (S16, S17, S19, S21, S23, S27) are located in the southern segment of the array, in Kunlun and Songpan–Ganzi. Fig. 6 allows seeing the stacked splitting measurements at each station belonging to a particular group (central panel), which are shown individually by bars drawn on concentric circles, in turn enclosed in rectangles at both sides of the central map. The radius of
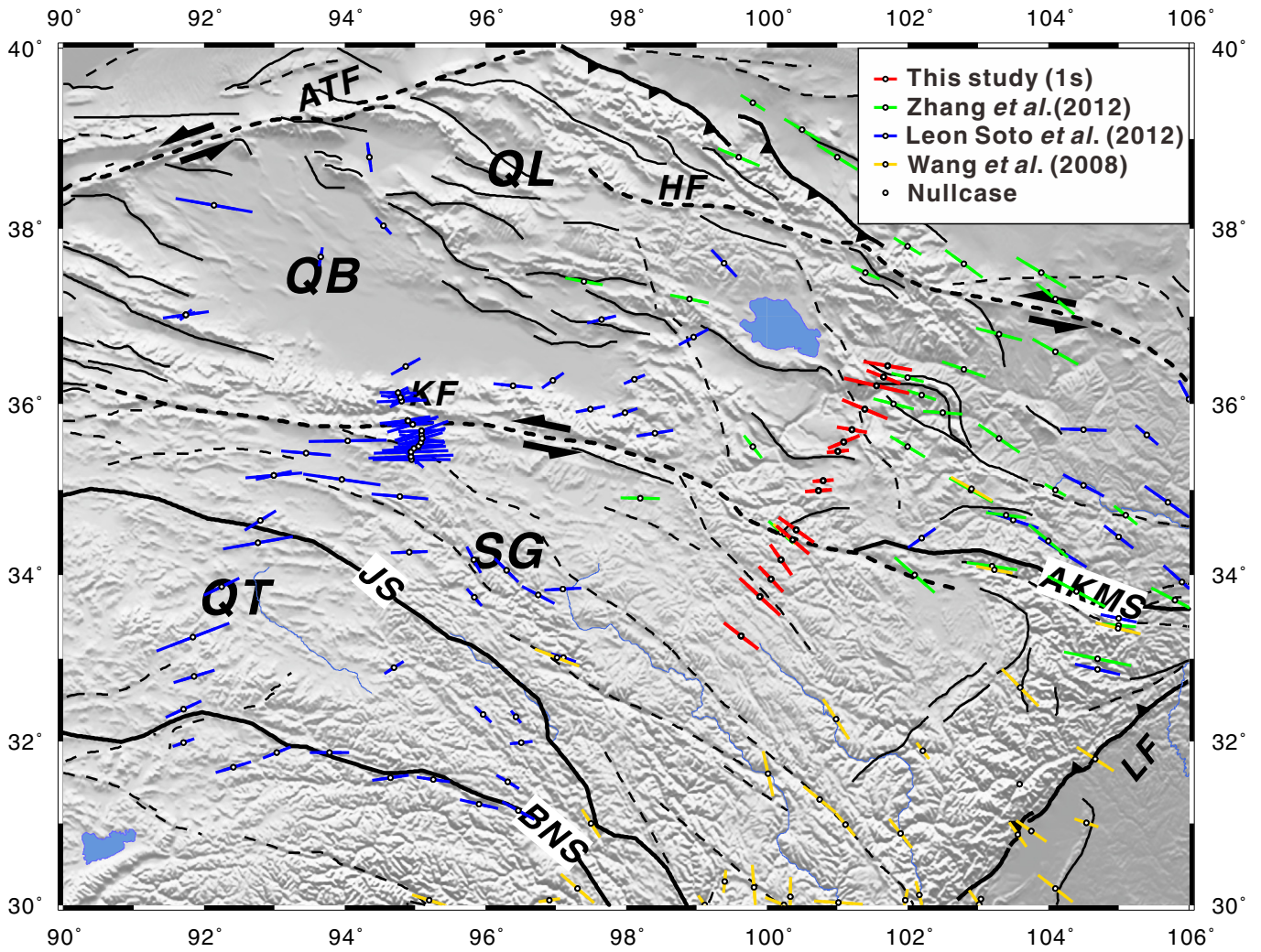
splitting parameters on back azimuths, and proposed a two-layer anisotropy model between Haiyuan and Kunlun fault. While Zhao et al. (2011) proposed the possible existence of a double-layer anisotropy with a dipping symmetry axis in the Qilian Mountain. Despite the azimuthal coverage with unevenly distributed earthquakes, which certainly introduces a difficulty factor to characterize the anisotropy structure beneath each array station, the results obtained in this study do not allow us to rule out the possibility of a complex anisotropy structure beneath the reference profile, which could be explained by anisotropy varying laterally (Alsina and Snieder, 1995; Liao et al., 2007; Savage and Sheehan, 2000), a dipping axis of symmetry (Hartog and Schwartz, 2000) or multiple layers of anisotropy (Silver and Savage, 1994). Due to the limited quantity of measurements and not distinct variation with back azimuths of each station, we stacked splitting measurements at each station using weighting

Fig. 5. Shear-wave splitting vectors (fast polarization directions and delay times) extracted from previous research works together with those obtained in this study (red bars, see top right inset); they are all drawn on a topographic map of the explored region. The direction and length of each vector indicate the fast direction and the splitting delay time, respectively. SKS splitting measurements were collected from Wang et al. (2008) (yellow bars), Leon Soto et al. (2012) (blue bars) and Zhang et al. (2012) (green bars). Acronyms are the same as in Fig. 1.

each of these circles indicates the ray parameter. The directions and lengths of the bars on the circles mean fast directions and magnitude of delay time, respectively. The averages of fast directions and delay times for group 1 are N103.8°E and 0.98 s. The measurement agrees

Table 4
Stacked shear-wave splitting measurements.

Station	λ_E (°)	φ_N (°)	φ (°)	σ_φ (°)	δt (s)	$\sigma_{\delta t}$ (s)	N
S00	101.72	36.44	100	41.9	1.34	0.67	3
S01	101.66	36.31	112	11.9	0.98	0.52	3
S02	101.56	36.21	103	0.7	1.86	0.21	2
S04	101.39	35.94	113	16.3	1.36	0.28	2
S06	101.21	35.70	100	29.7	0.80	0.57	2
S07	101.09	35.56	68	18.2	0.91	0.41	4
S08	101.01	35.45	84	12.6	0.57	0.45	3
S11	100.80	35.11	86	0.0	0.54	0.14	2
S12	100.73	34.99	86	12.7	0.71	0.14	2
S16	100.42	34.53	126	7.2	1.19	0.16	3
S17	100.37	34.41	131	31.6	1.20	0.21	4
S19	100.20	34.18	145	7.0	1.00	0.15	1
S21	100.06	33.95	136	11.0	0.96	0.18	9
S23	99.90	33.74	133	3.2	1.52	0.23	8
S27	99.63	33.27	128	10.5	1.17	0.58	6

Nomenclature: λ_E, latitude; φ_N, longitude; φ, fast polarization direction; σ_φ, measurement error; δt, delay time; $\sigma_{\delta t}$, measurement error; N, number of measurements.

well with the results provided by Zhang et al. (2012) for station LJX (104.275 ± 10.486°, 1.158 ± 0.674 s), station QSS (105.332 ± 6.780°, 0.931 ± 0.321 s) and station HUL (107.6862 ± 23.475°, 0.813 ± 0.402 s), which are located near the stations of group 1. The averages calculated for group 2 are N83.2°E and 0.63 s, while the averages for group 3 calculated with the largest number of measurements (31) are N132.3°E and 1.10 s. Our results are consistent with those supplied by Wang et al. (2008) and Zhang et al. (2012) for station MAQ (131.8 ± 3°, 0.82 ± 0.1 s) and station DAW (131.916 ± 10.463°, 0.923 ± 0.152 s) which are located in the vicinity of stations of group 3. Unlike group 1 and group 3, group 2 shows an anisotropy structure completely differentiated from that of the other two groups, both with respect to fast polarization directions and delay times, especially an obvious fall in delay times.

In the case of a homogeneous anisotropic medium with a horizontal symmetry axis, nulls can be interpreted as potential fast or slow polarization directions assuming that the wave arrives with an initial polarization at the same direction of the symmetry axis, which results in no shear wave splitting (Silver and Savage, 1994). If so, the back azimuths of events that give nulls for potential fast or slow polarization directions at stations of groups 1 and 3 suggest by sub-parallelism how is locally orientated the horizontal symmetry axis. While there exists a differential angle of about 20–40° between fast directions and the back azimuths of events calculated at stations of group 2 (Table 3).
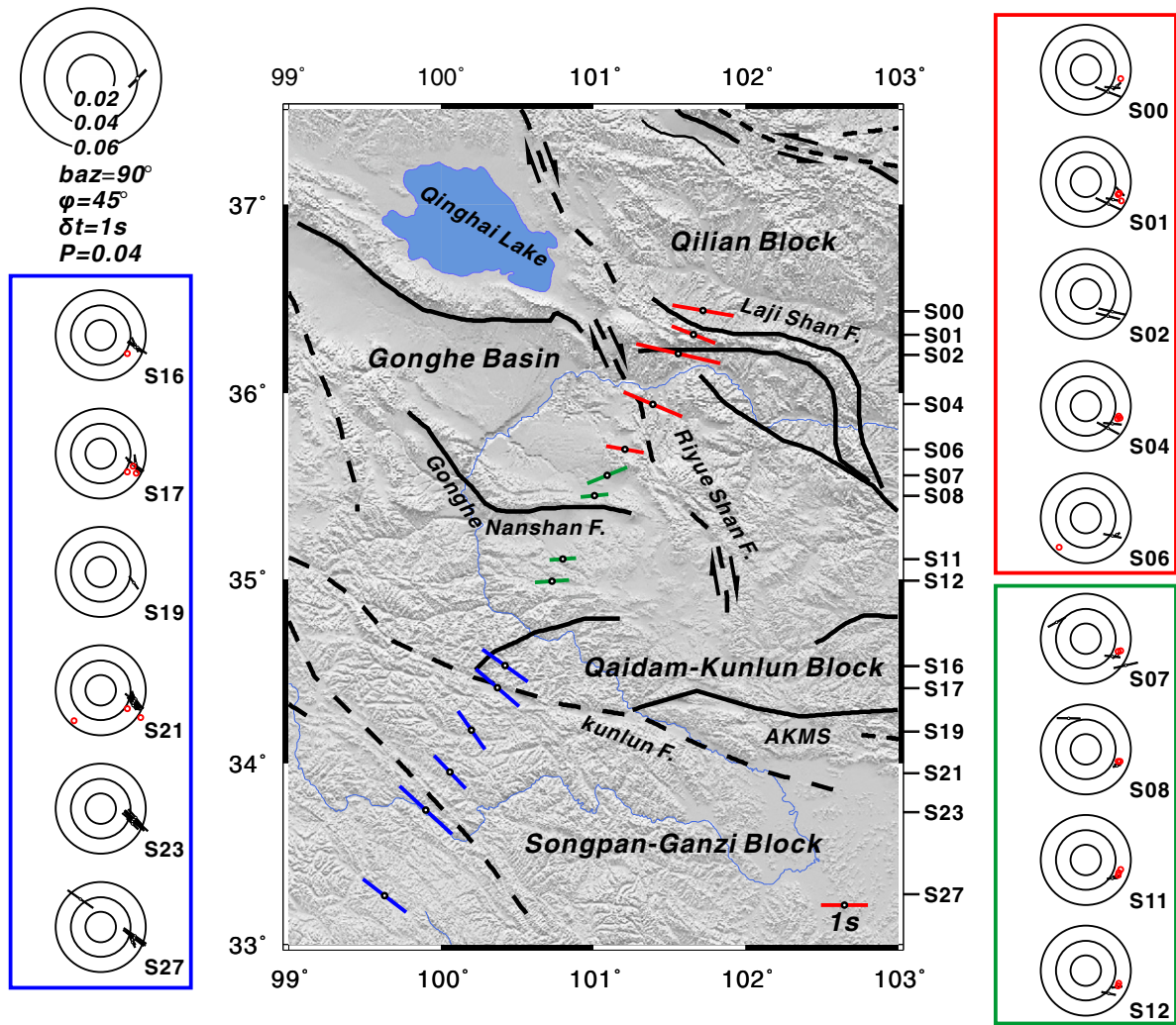
Fig. 6. Splitting parameters obtained in this study and represented by vectors in the zoomed explored area. The direction and length of each vector indicate the fast direction and the splitting delay time, respectively. Red bars refer to stations of group 1 (northern third of the array), green bars to stations of group 2 (middle third of the array) and blue bars to stations of group 3 (southern third of the array). The splitting parameters at each station group are shown by bars drawn on individual concentric circles, in turn enclosed in rectangles at both sides of the central map. The radius of each of these circles indicates the ray parameter. The directions and lengths of the bars on the circles mean fast polarization directions and magnitude of delay time, respectively.

4. Discussion

4.1. Anisotropy source

The measurement is the integrated result from core–mantle boundary to the station along the source-receiver path. The contribution of various layers of the Earth to SKS delay times has been investigated by Silver (1996). The study (Silver, 1996) shows that the average contribution from the crust is 0.2 s, and the contribution from the lower mantle and the transition zone is also less than 0.2 s. Beneath northern Tibet, Herquel et al. (1995) found that the strength of crustal anisotropy is about 0.2–0.3 s. The delay times of crustal anisotropy in some other parts of Tibet are also less than 0.3 s (Chen et al., 2013; McNamara and Owens, 1993; Sun et al., 2011). With a similar crustal thickness to that of northern Tibet in the study area the contribution of the crust may be no more than 0.3 s. In our individual measurements, the delay times at our stations range from 0.4 s (station S08) to 2.0 s (station S27) and more than 80% of them are equal to or greater than 0.8 s (Table 2). In our station averages, most are above 0.8 s with exception of a few stations (0.54, 0.57 and 0.71 s) (Table 4). These times are too large to be considered with origin in the crust, so that it is quite reasonable to infer that the

main source of the observed anisotropy is rather located in the upper mantle.

Since the upper mantle includes the mantle lithosphere and the underlying channel of the asthenosphere, the question is whether the anisotropy obtained from SKS/SKKS splitting analysis exists in the mantle lithosphere, the asthenosphere or in both layers. To test the simple asthenospheric flow model, we compare the fast polarization directions with that of the absolute plate motion (APM). In the case of coupling with the underlying asthenosphere, the APM direction should be coherent with the motion of the asthenosphere flow.

Table 5
Anisotropic layer thicknesses based on delay times sorted by group of stations, compared with crustal thickness and lithospheric thickness.

	Delay time	Anisotropic layer thickness	Crustal thickness	Lithospheric thickness
Group 1	0.98 s	110 km	56 km	150 km
Group 2	0.63 s	71 km	59 km	150 km
Group 3	1.10 s	124 km	61 km	125 km

Assumptions: 4% of anisotropy and shear velocity of 4.5 km/s. The thicknesses of the crust and the lithosphere are obtained from P and S receiver functions separately (Xu et al., 2014; Zhang et al., 2012).

In the hot-spot frame, the HS3-NUVEL1a model (Gripp and Gordon, 2002) predicts a coherent APM direction of ~N282°E ± 2° in the study area, which does not match the observed spatial change of fast directions in the whole area, although it is subparallel to the average fast direction for group 1. This means that a simple uniform mantle convection model is unsuitable to explain the complex splitting observations in the study area.

In order to determine the contribution of the mantle lithosphere and/or the asthenosphere to the anisotropy, we can estimate the anisotropic layer thickness to then compare it with those of the crust and lithosphere. If we assume that the observed anisotropy is from a single layer of anisotropic media, the apparent thickness of the layer can be estimated by $H = \delta t \cdot \beta_0 / \delta\beta$, where δt is the observed shear wave delay time, β_0 is the shear velocity of isotropic layer and $\delta\beta$ is the velocity difference between the fast and slow direction (Silver, 1996). In our case, we select $\beta_0 = 4.5$ km/s, and $\delta\beta = 4\%$. The thicknesses of the crust and lithosphere are obtained separately from P and S receiver functions (Xu et al., 2014; Zhang et al., 2012). These results are given in Table 5 for each of the segments that make up the reference profile. The thickness of the lithosphere beneath group 1 is probably around 150 km (Zhang et al., 2012), assuming an average 56 km crust thickness (Xu et al., 2014), and the mantle lithospheric thickness is about 94 km. Since the anisotropic layer has a thickness of about 110 km, this implies that the observed anisotropy resides mainly in the mantle lithosphere. In a similar way, we can deduce that the anisotropy seems to come from mantle lithosphere as well as asthenosphere beneath the stations of group 3; in change, beneath the stations of group 2, the thickness of lithosphere is enough to produce the anisotropy.

4.2. Anisotropy patterns across the Kunlun fault

Across the middle part of the Kunlun fault, different splitting parameters were observed by previous studies. Eken et al. (2013) suggests that the fast polarization directions are largely parallel to the major strike–slip structures in Kunlun Shan and north of Songpan–Ganzi, while a dramatic decreasing in delay times even null cases result to be somewhat characteristic of the area north of the Kunlun fault possibly due to a thin anisotropic layer or weak anisotropy, which is similar with Leon Soto et al. (2012).

We have also measured different splitting parameters across the Kunlun fault. The fast polarization directions determined at stations of group 3 mostly located south of the Kunlun fault are subparallel to the major strike–slip structures and also relate closely to the surface geological features observed on the topographic map. Additionally, they also agree well with the finite-strain left-lateral simple shear direction deduced from GPS observations in agreement with Wang et al. (2008). We interpret these facts as evidence for vertically coherent deformation of the upper crust and the mantle lithosphere. The lack of any obvious trend in delay times on the plateau supports the idea that the deformation is distributed throughout Tibet (thin-sheet model) rather than being focused along block boundaries. Across Kunlun fault, the fast direction determined at stations of group 2 exhibits an abrupt change of 50° counterclockwise (Fig. 6) passing from a mean value of N132.3°E to N83.2°E, and the delay time also reflects a remarkable decreasing from 1.10 s to 0.63 s. The small delay times may result from weak anisotropy due to the smaller amount of deformation experienced by the lithosphere, which is inferred from the low seismic activity in this area (Xu et al., 2014).

4.3. Geodynamic model of upper mantle deformation

Associated with the India–Eurasia collision, NNE–SSW or NE–SW compression in northeastern Tibet could cause axes approximately orientated northwest–southeast for the structural olivine and thus explain our observations of fast directions at stations of groups 1 and 3

(Heidbach et al., 2010; Tian and Santosh, 2015; Xu, 2001; Xu et al., 2008). Nevertheless, a noteworthy point is that there is a difference of about 30° between them (Fig. 6). However, the fast directions at stations of group 2 do not seem to keep any correlation with the stress field in this zone, and the delay times are much smaller than those of groups 1 and 3 (Fig. 6).

Along the profile the crustal Vp/Vs ratios have been calculated from receiver functions (Fig. 7a, Xu et al., 2014). The values of group 1 and group 3 show higher than that of group 2. The lateral variation of crustal Vp/Vs ratios may be the deputy of rock composition and temperature. If the high value of crustal Vp/Vs ratio is resulted from warm lithosphere, the lithosphere beneath group 1 and group 3 is easy to deform and produce large delay time, which is marked in red color in Fig. 7a; in contrast, that beneath group 2 may be a cold lithosphere which is difficult to deform and present weak anisotropy, marked in blue color in Fig. 7a.

Bearing in mind the shear-wave splitting measurements, we propose a schematic model to explain the stress regime affecting the study area, which essentially is based on its segmented anisotropy structure (Fig. 7b). We suggest that there may be ladder-shaped folded structure with colder maybe stronger lithosphere beneath the middle transect of the reference profile than beneath the other two transects, which supposes an obstacle to the deformation of the lithosphere. As a result, the fast polarization direction rotates about 30° counterclockwise
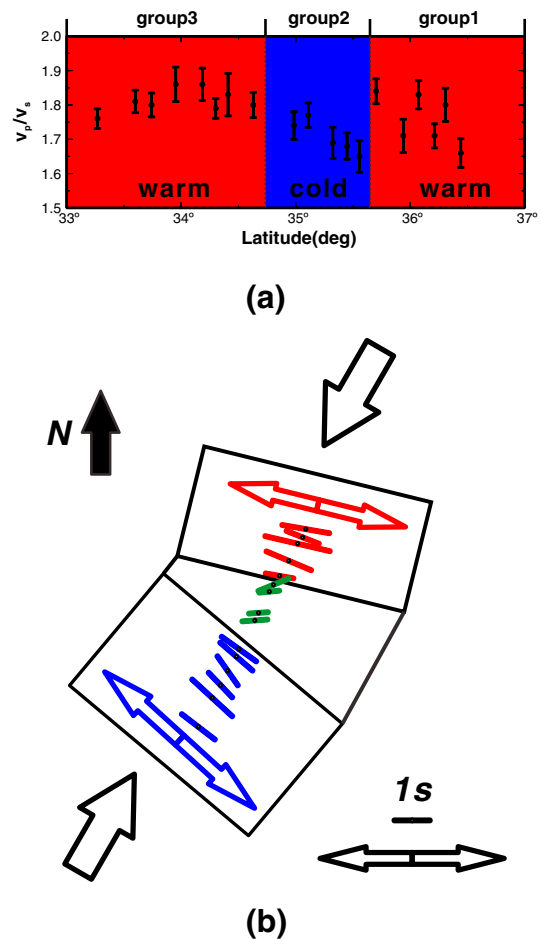

(a)

(b)

Fig. 7. (a) Vp/Vs ratio values with error bars for each of the three groups of stations installed at different latitudes. The red and blue colors represent warm and cold lithosphere respectively. (b) Schematic model proposed to explain the stress regime derived from shear-wave splitting results. The bars of different colors represent SKS-wave splitting measurements for each of the three station groups mentioned in Fig. 6. The delay time scale is included in the bottom right angle. The hollow double-headed arrows stand for averages of splitting parameters for each transect, while the hollow arrows with a single head indicate the dominant compression regime.

when passing from the southern segment (group 3) to the segment further north (group 1) in NE direction (Fig. 7b). In the illustration, the splitting vectors are taken from Fig. 6; the hollow double-headed arrows stand for averages of splitting parameters for each transect, while the hollow arrows with a single head indicate the dominant compression regime.

5. Conclusions

In this study shear-wave splitting measurements have been performed from SKS and SKKS phases recorded at 15 broadband seismographic stations deployed perpendicularly to the fault, and a distinct variation of seismic splitting parameters is shown across the Kunlun fault. A possible deformation pattern of upper mantle is used to explain our observation.

The average splitting parameters of the southern segment in Songpan–Ganzi block are N132.3°E and 1.1 s respectively, and those of the northern segment in Qilian block are N103.8°E and 0.98 s, interfered with the middle segment in the Qaidam–Kunlun block with a smaller average delay time 0.63 s. The model outlines a ladder-shaped folded structure with colder maybe stronger lithosphere beneath the middle transect of the reference profile than beneath the other two transects, which implies an obstacle to the deformation across the Kunlun fault, which results in a counterclockwise rotation of the fast direction of about 30° accompanied by smaller delay time values when going northward.

More seismic events distributed on a wider azimuthal range and a greater number of shear-wave splitting measurements would likely lead to a more accurate knowledge of the complex anisotropy structure of the region and its deformation.

Acknowledgements

Appendix A. Supplementary data

Supplementary data to this article can be found online at http://dx.doi.org/10.1016/j.tecto.2015.07.030.

References

Alsina, D., Snieder, R., 1995. Small-scale sublithospheric continental mantle deformation-constraints from sks splitting observations. Geophys. J. Int. 123, 431–448.
Avouac, J.-P., Tapponnier, P., 1993. Kinematic model of active deformation in central-Asia. Geophys. Res. Lett. 20, 895–898.
Bowman, J.R., Ando, M., 1987. Shear-wave splitting in the upper-mantle wedge above the Tonga subduction zone. Geophys. J. R. Astron. Soc. 88, 25–41.
Chang, L.-J., Wang, C.-Y., Ding, Z.-F., Zhou, M.-D., Yang, J.-S., Xu, Z.-Q., Jiang, X.-D., Zheng, X.-F., 2008. Seismic anisotropy of upper mantle in the northeastern margin of the Tibetan Plateau. Chin. J. Geochem. 51, 431–438.

Chen, Y., Zhang, Z., Sun, C., Badal, J., 2013. Crustal anisotropy from Moho converted Ps wave splitting analysis and geodynamic implications beneath the eastern margin of Tibet and surrounding regions. Gondwana Res. 24, 946–957.
Chevrot, S., Favier, N., Komatitsch, D., 2004. Shear wave splitting in three-dimensional anisotropic media. Geophys. J. Int. 159, 711–720.
Clark, M.K., Royden, L.H., 2000. Topographic ooze: building the eastern margin of Tibet by lower crustal flow. Geology 28, 703–706.
Dayem, K.E., Molnar, P., Clark, M.K., Houseman, G.A., 2009. Far-field lithospheric deformation in Tibet during continental collision. Tectonics 28, TC6005.
Deng, Y., Shen, W., Xu, T., Ritewoller, M.H., 2015. Crustal layering in northeastern Tibet: a case study based on joint inversion of receiver functions and surface wave dispersion. Geophys. J. Int. http://dx.doi.org/10.1093/gji/ggv1321 (in press).
Eken, T., Tilmann, F., Mechie, J., Zhao, W., Kind, R., Su, H., Xue, G., Karplus, M., 2013. Seismic Anisotropy from SKS Splitting beneath Northeastern Tibet. Bull. Seismol. Soc. Am. 103, 3362–3371.
England, P., McKenzie, D., 1982. A thin viscous sheet model for continental deformation. Geophys. J. R. Astron. Soc. 70, 295–321.
Favier, N., Chevrot, S., 2003. Sensitivity kernels for shear wave splitting in transverse isotropic media (vol 153, pg 213, 2003). Geophys. J. Int. 154, 595-595.
Fu, B., Awata, Y., 2007. Displacement and timing of left-lateral faulting in the Kunlun Fault Zone, northern Tibet, inferred from geologic and geomorphic features. J. Asian Earth Sci. 29, 253–265.
Galassi, M., Davies, J., Theiler, J., Gough, B., Jungman, G., Booth, M., Rossi, F., 2007. GNU Scientific Library Reference Manual. Network Theory Ltd., Bristol, U.K. (251 pp.).
Gripp, A.E., Gordon, R.G., 2002. Young tracks of hotspots and current plate velocities. Geophys. J. Int. 150, 321–361.
Hartog, R., Schwartz, S.Y., 2000. Subduction-induced strain in the upper mantle east of the Mendocino triple junction, California. J. Geophys. Res. Solid Earth 105, 7909–7930.
Heidbach, O., Tingay, M., Barth, A., Reinecker, J., Kurfess, D., Mueller, B., 2010. Global crustal stress pattern based on the World Stress Map database release 2008. Tectonophysics 482, 3–15.
Herquel, G., Wittlinger, G., Guilbert, J., 1995. Anisotropy and crustal thickness of northern-Tibet—new constraints for tectonic modeling. Geophys. Res. Lett. 22, 1925–1928.
Herquel, G., Tapponnier, P., Wittlinger, G., Mei, J., Danian, S., 1999. Teleseismic shear wave splitting and lithospheric beneath and across the Altyn Tagh fault. Geophys. Res. Lett. 26, 3225–3228.
Huang, Z., Wang, L., Zhao, D., Mia, N., Xu, M., 2011. Seismic anisotropy and mantle dynamics beneath China. Earth Planet. Sci. Lett. 306, 105–117.
Kirby, E., Harkins, N., Wang, E., Shi, X., Fan, C., Burbank, D., 2007. Slip rate gradients along the eastern Kunlun fault. Tectonics 26, TC2010.
Leon Soto, G., Sandvol, E., Ni, J.F., Flesch, L., Hearn, T.M., Tilmann, F., Chen, J., Brown, L.D., 2012. Significant and vertically coherent seismic anisotropy beneath eastern Tibet. J. Geophys. Res. Solid Earth 117, B05308.
Li, J., Wang, X., Niu, F., 2011a. Seismic anisotropy and implications for mantle deformation beneath the NE margin of the Tibet plateau and Ordos plateau. Phys. Earth Planet. Inter. 189, 157–170.
Li, Y., Wu, Q., Zhang, F., Feng, Q., Zhang, R., 2011b. Seismic anisotropy of the Northeastern Tibetan Plateau from shear wave splitting analysis. Earth Planet. Sci. Lett. 304, 147–157.
Liao, W.-L., Ding, Z.-F., Zeng, R.-S., Zhang, H., 2007. Shear wave splitting in Himalaya. Chin. J. Geochem. 50, 1437–1447.
Long, M.D., van der Hilst, R.D., 2005. Estimating shear-wave splitting parameters from broadband recordings in Japan: a comparison of three methods. Bull. Seismol. Soc. Am. 95, 1346–1358.
Long, M.D., van der Hilst, R.D., 2006. Shear wave splitting from local events beneath the Ryukyu arc: trench-parallel anisotropy in the mantle wedge. Phys. Earth Planet. Inter. 155, 300–312.
McNamara, D.E., Owens, T.J., 1993. Azimuthal shear-wave velocity anisotropy in the basin and range province using Moho PS converted phases. J. Geophys. Res. Solid Earth 98, 12003–12017.
Meyer, B., Tapponnier, P., Bourjot, L., Metivier, F., Gaudemer, Y., Peltzer, G., Shunmin, G., Zhitai, C., 1998. Crustal thickening in Gansu-Qinghai, lithospheric mantle subduction, and oblique, strike–slip controlled growth of the Tibet plateau. Geophys. J. Int. 135, 1–47.
Royden, L., 1996. Coupling and decoupling of crust and mantle in convergent orogens: implications for strain partitioning in the crust. J. Geophys. Res. Solid Earth 101, 17679–17705.
Savage, M.K., 1999. Seismic anisotropy and mantle deformation: what have we learned from shear wave splitting? Rev. Geophys. 37, 65–106.
Savage, M.K., Sheehan, A.F., 2000. Seismic anisotropy and mantle flow from the Great Basin to the Great Plains, western United States. J. Geophys. Res. Solid Earth 105, 13715–13734.
Silver, P.G., 1996. Seismic anisotropy beneath the continents: probing the depths of geology. Annu. Rev. Earth Planet. Sci. 24, 385–432.
Silver, P.G., Chan, W.W., 1991. Shear-wave splitting and subcontinental mantle deformation. J. Geophys. Res. Solid Earth 96, 16429–16454.
Silver, P.G., Savage, M.K., 1994. The interpretation of shear-wave splitting parameters in the presence of 2 anisotropic layers. Geophys. J. Int. 119, 949–963.
Sun, C.-Q., Chen, Y., Gao, E.-G., 2011. The crustal anisotropy and its geodynamical significance of the strong basin-range interaction zone beneath the east margin of Qinghai-Tibet plateau. Chin. J. Geochem. 54, 1205–1214.
Tapponnier, P., Peltzer, G., Ledain, A.Y., Armijo, R., Cobbold, P., 1982. Propagating extrusion tectonics in Asia—new insights from simple experiments with plasticine. Geology 10, 611–616.
Tapponnier, P., Meyer, B., Avouac, J.P., Peltzer, G., Gaudemer, Y., Guo, S.M., Xiang, H.F., Yin, K.L., Chen, Z.T., Cai, S.H., Dai, H.G., 1990. Active thrusting and folding in the Qilian-

shan, and decoupling between upper crust and mantle in northeastern Tibet. Earth Planet. Sci. Lett. 97, 382–403.

Tapponnier, P., Xu, Z.Q., Roger, F., Meyer, B., Arnaud, N., Wittlinger, G., Yang, J.S., 2001. Geology—oblique stepwise rise and growth of the Tibet plateau. Science 294, 1671–1677.

Tian, X., Santosh, M., 2015. Fossilized lithospheric deformation revealed by teleseismic shear wave splitting in eastern China. GSA Today 25, 4–10.

Tian, X., Zhang, Z., 2013. Bulk crustal properties in NE Tibet and their implications for deformation model. Gondwana Res. 24, 548–559.

Tian, X., Zhang, J., Si, S., Wang, J., Chen, Y., Zhang, Z., 2011. SKS splitting measurements with horizontal component misalignment. Geophys. J. Int. 185, 329–340.

Van der Woerd, J., Ryerson, F.J., Tapponnier, P., Meriaux, A.S., Gaudemer, Y., Meyer, B., Finkel, R.C., Caffee, M.W., Zhao, G.G., Xu, Z.Q., 2000. Uniform Slip-Rate along the Kunlun Fault: implications for seismic behaviour and large-scale tectonics. Geophys. Res. Lett. 27, 2353–2356.

Van Der Woerd, J., Tapponnier, P., Ryerson, F.J., Meriaux, A.S., Meyer, B., Gaudemer, Y., Finkel, R.C., Caffee, M.W., Zhao, G.G., Xu, Z.Q., 2002. Uniform postglacial slip-rate along the central 600 km of the Kunlun Fault (Tibet), from 26Al, 10Be, and 14C dating of riser offsets, and climatic origin of the regional morphology. Geophys. J. Int. 148, 356–388.

Wang, C.-Y., Flesch, L.M., Silver, P.G., Chang, L.-J., Chan, W.W., 2008. Evidence for mechanically coupled lithosphere in central Asia and resulting implications. Geology 36, 363–366.

Wu, Z., Xu, T., Badal, J., Yao, H., Wu, C., Zhang, Z., Teng, J., 2015. Shear-wave velocity structure of the crust in northeastern Tibet revealed by ambient seismic noise and receiver functions. Gondwana Res. (in press).

Wüstefeld, A., Bokelmann, G., 2007. Null detection in shear-wave splitting measurements. Bull. Seismol. Soc. Am. 97, 1204–1211.

Xu, Z.H., 2001. A present-day tectonic stress map for eastern Asia region. Acta Seismol. Sin. 23, 492–501.

Xu, J.R., Zhao, Z.X., Ishkawa, Y., 2008. Regional characteristics of crustal stress field and tectonic motions in and around Chinese mainland. Chin. J. Geochem. 51, 770–781.

Xu, T., Wu, Z., Zhang, Z., Tian, X., Deng, Y., Wu, C., Teng, J., 2014. Crustal structure across the Kunlun fault from passive source seismic profiling in East Tibet. Tectonophysics 627, 98–107.

Yin, A., Dang, Y., Zhang, M., McRivette, M.W., Burgess, W.P., Chen, X., 2007. Cenozoic tectonic evolution of Qaidam basin and its surrounding regions (part 2): wedge tectonics in southern Qaidam basin and the Eastern Kunlun Range. Geol. Soc. Am. Spec. Pap. 433, 369–390.

Yin, A., Dang, Y.-Q., Wang, L.-C., Jiang, W.-M., Zhou, S.-P., Chen, X.-H., Gehrels, G.E., McRivette, M.W., 2008a. Cenozoic tectonic evolution of Qaidam basin and its surrounding regions (Part 1): the southern Qilian Shan-Nan Shan thrust belt and northern Qaidam basin. Geol. Soc. Am. Bull. 120, 813–846.

Yin, A., Dang, Y.-Q., Zhang, M., Chen, X.-H., McRivette, M.W., 2008b. Cenozoic tectonic evolution of the Qaidam basin and its surrounding regions (Part 3): structural geology, sedimentation, and regional tectonic reconstruction. Geol. Soc. Am. Bull. 120, 847–876.

Zhang, Z., Klemperer, S., Bai, Z., Chen, Y., Teng, J., 2011. Crustal structure of the Paleozoic Kunlun orogeny from an active-source seismic profile between Moba and Guide in East Tibet, China. Gondwana Res. 19, 994–1007.

Zhang, H., Teng, J., Tian, X., Zhang, Z., Gao, R., Liu, J., 2012. Lithospheric thickness and upper-mantle deformation beneath the NE Tibetan Plateau inferred from S receiver functions and SKS splitting measurements. Geophys. J. Int. 191, 1285–1294.

Zhao, L., Xue, M., 2015. An observation related to directional attenuation of SKS waves propagating in anisotropic media. Geophys. J. Int. 201, 276–290.

Zhao, L., Zheng, T., Lu, G., Ai, Y., 2011. No direct correlation of mantle flow beneath the North China Craton to the India–Eurasia collision: constraints from new SKS wave splitting measurements. Geophys. J. Int. 187, 1027–1037.